

Reciprocal frame design for large-scale timber construction

Received: 25 July 2024

Accepted: 6 November 2025

Published online: 12 December 2025

 Check for updates

Peiqi Xu^{1,2,6}, Pengyang Zhao^{2,6}, Bo Xia³, Zhenyu Zhao⁴, Nianxiong Liu^{①,2}✉, Shuyang Zhang^②✉ & Jianbin Du^{③,5}✉

Timber structures are attracting increasing interest due to their sustainability, especially as reinforced concrete proves less durable and more environmentally harmful than expected. However, the availability of large-scale timber suitable for modern structural engineering remains limited. Reciprocal frames, which use small components to span large areas, offer architectural possibilities in timber construction but are constrained by limited curve adaptability and insufficient structural performance. Here, we introduce a reciprocal frame configuration that enhances morphological adaptability and structural redundancy. The design preserves the benefits of small-scale modularity and large-span capability while enabling rapid deployment, cost-efficiency, and improved structural integrity. It offers a renewable, low-cost, and flexible solution for large-scale construction.

Reciprocal frame (RF) is a specialized structural configuration with a rich historical heritage¹, known in both Eastern and Western traditional applications. Classic examples include Leonardo da Vinci's "tessere al pont (woven bridge)" sketch² from the Renaissance in the West (Fig. 1a) and the Rainbow Bridge³ from the Song Dynasty in the East (Fig. 1c). The primary aim of employing a reciprocal system was to build bridges over rivers without using columns⁴. Confronted with the scarcity of large timbers, ancient craftsmen utilized smaller-scale materials to collaboratively form structures capable of spanning large distances⁴. In traditional RF system, the mechanism for transmitting forces operates in a cyclical pattern: the first set of components supports the hinge joints from the second set through bending moments, while the hinge joints from the first set are simultaneously strengthened by the bending moments of the second set⁵ (Fig. 1b). Essentially, the primary purpose of reciprocal behavior in traditional applications is structural reinforcement, thereby enhancing the span and load-bearing capacity of the construction (Fig. 1d).

Modernism has made the design and construction of large-span, free-form surfaces a significant category in architectural engineering⁶. In response to the morphological limitations of arches and to meet contemporary design requirements, the structural principles of the RF

system have undergone a profound transformation. Instead of reinforcing each other, the components are now configured into planar-like structural units, aimed at keeping balance on free-form surfaces⁵ (Fig. 1e). This principle has resulted in a general lack of structural redundancy in contemporary RF systems, where the failure of a single member can lead to the collapse of the entire structure^{7–9}. This issue is illustrated by the types of RF applications seen over recent decades, which have predominantly featured landscaped pavilions and small-scale residential projects (Fig. 1), with limited application in large-scale buildings such as commercial or sports facilities^{10–13}. This can be attributed to the contemporary equilibrium-oriented reciprocal behavior, which deviates from the original purpose of structural reinforcement, and is insufficient to provide the necessary redundancy for large-scale projects (see supplementary file Fig.1 for more cases classification). Consequently, contemporary RF applications have become more like artifacts (Fig. 1f), which are valued for their structural expressiveness rather than their engineering utility^{14,15}. They are less dominant and have been gradually replaced by weaving systems in current architectural and engineering practices.

Traditional RF systems were designed for unidirectional arched surfaces¹⁶. Although contemporary RF systems have diverged from the

¹School of Architecture, Tianjin University, Tianjin, PR China. ²School of Architecture, Tsinghua University, Beijing, PR China. ³School of Aerospace Engineering, Tsinghua University, Beijing, PR China. ⁴Department of Automation, Tsinghua University, Beijing, PR China. ⁵State Key Laboratory of Flexible Electronics Technology, Tsinghua University, Beijing, PR China. ⁶These authors contributed equally: Peiqi Xu, Pengyang Zhao.

✉ e-mail: phlnx@tsinghua.edu.cn; zhangshu20@tsinghua.org.cn; dujb@tsinghua.edu.cn

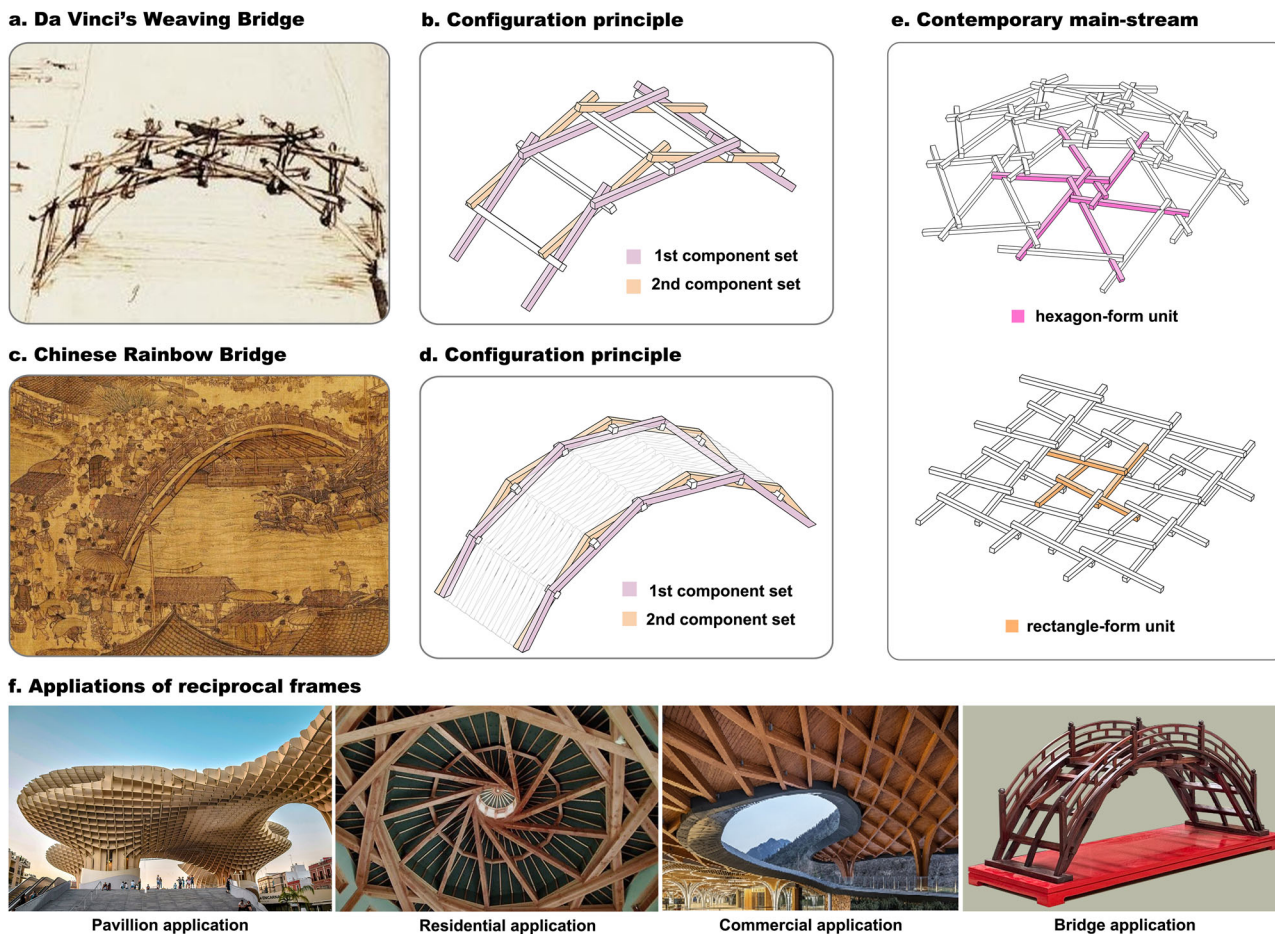


Fig. 1 | Evolution of reciprocal frame (RF) structures. **a** Leonardo da Vinci's woven bridge sketch in Codex Atlanticus represents one of the most famous RF concepts in the Western world, where components are supposed to be tied together at nodes. **b** In da Vinci's weaving bridge, the node of the second component set is supported by the bending moment of the first set via vertical elements, and vice versa, achieving mutual reinforcement. **c** An early RF practice in the East is the Rainbow Bridge depicted in "Along the River During the Qingming Festival", and the bridge achieved a span of approximately 19.4 meters. **d** The Rainbow Bridge also features reciprocal behavior between the first and second component sets

through vertical elements. Its structural logic is relatively advanced as a realized application: components from one set (except the vertical elements) are connected as one. **e** Contemporary reciprocal frames have evolved into planar-like structural units, shifting the reciprocal behavior of components from reinforcement to maintaining equilibrium and adapting to more free-form shapes. **f** This evolution led to widespread RF applications, particularly in landscaped pavilions and residences. The shift sacrifices structural redundancy, resulting in instability if one single component fails.

original reciprocal purpose and compromised on structural redundancy to adapt to free-form surfaces. However, their ability to adapt to curvature changes in surfaces is still quite limited.¹⁷ This limitation arises because changes in the global frame are incrementally accumulated through numerous staggered angles between components in planar-like RF units (Fig. 1e). Therefore, contemporary RF system finds it challenging to accommodate significant curvature changes on the surface – large curvature may cause contactless between the planar-like units, thereby compromising on force transfer between components, rendering the reciprocal behavior and even the structural frame invalid. Among the 94 contemporary RF built cases collected, the maximum span-to-arch ratio is only 2.28, and the minimum normal radius of curvature is only 16.55 m. These figures clearly show the difficulty for the system to manage significant curvature variations and its constrained adaptability to highly variable surfaces (see Supplementary File Table 1 for the data collection of 94 RF cases).

With the design development of freeform structure, the generation of complex geometries and non-standard components has become increasingly feasible. However, constructability remains a critical factor limiting the practical application of such structures. In the context of RF systems, the structural components are designed to

maintain the same structural hierarchy¹⁸. While it allows for more uniform and dispersed force transfer, the actual construction process involves a complex sequence of component assemblies^{19,20}. Moreover, the interlocking joinery between components in RF systems establishes a tight coupling between the construction outcome and the design of physical connections, thereby necessitating explicit consideration and optimization of constructability – including the potential for standardized fabrication.

Furthermore, incorporating constructability-related criteria into the structural optimization process not only enhances engineering applicability but also effectively reduces construction costs²¹. For example, Cucuzza proposed improving the constructability of steel truss structures through component standardization and grouping strategies, and significantly reduced material waste by integrating cutting stock optimization methods²². Accordingly, in the intelligent design of complex structures such as RF systems, it is crucial to balance morphological freedom with construction feasibility in order to fulfill technical requirements beyond mere geometry²³.

In this work, we propose a tessere-inspired RF configuration based on traditional reinforced RF principles, expanding free-form surface adaptability with structural redundancy. Based on the interdisciplinary

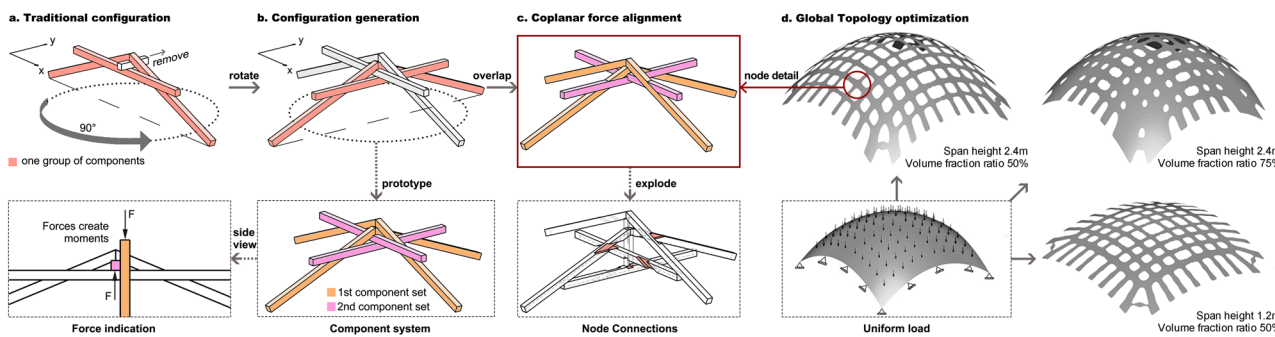


Fig. 2 | Reciprocal frame(RF) prototype formation. **a** Traditional RF node prototype, consisting of the first system, the second system, and the vertical system. **b** Extension of traditional RF nodes in perpendicular directions. The vertical system comprises the first and also the second system, and enables effective force transmission across both axes, increasing structural redundancy, but the misaligned forces create moments within the node. **c** To avoid moments at the node, the two system components along the same axis are overlapped, establishing interlocking

connections through tenon-and-mortise joints. **d** Topology optimization configurations of thin-walled shell structures under approximately uniform loads. Changing the height of the shell structure (2.4 m and 1.2 m) and the constraint volume fraction (50% and 75%), the material of the topology optimization configuration of the structures under approximately uniform loads all exhibit orthogonal distributions, which indicates that the orthogonal configuration achieves the highest efficiency in force transmission.

methodology that synergizes architecture and structural engineering²⁴, we demonstrate the feasibility of this configuration in terms of morphology generation and structural performance, adopting a combination of parametric form modeling and structural finite element analysis. Furthermore, we systematically incorporate a constructability-oriented design and optimization mechanism. Based on the composition rules of the RF configuration^{25–27}, we rationalize the assembly principles through a parametric approach. In addition, Computer Numerical Control (CNC) manufacturing and robotic assembly techniques are introduced to automate the construction process. This approach significantly mitigates assembly complexity and enhances overall constructability.

In summary, this study establishes a comprehensive design system to address morphological adaptability, structural redundancy, and construction issues. This research mitigates the inherent limitations of timber structures, including high costs, limited spans, slow deployment, simplistic morphology, and inadequate structural performance^{28,29}. Moreover, the RF configuration design not only presents cost reduction, flexibility, adaptability, time efficiency in civil engineering but also reveals broader potential in aerospace engineering and mechanical engineering.

Results

General concepts of the RF configuration

Although the traditional RF system exhibits limited morphological adaptability, the structural redundancy embedded in its configuration provides valuable insights. In the tessere il pont (Fig. 1b), the configuration prototype that carries the reciprocal behavior consists of 3 parts: 2 sets of components (3 rods in total) intersecting to form a triangle, with another component inserted perpendicularly in the triangle. Multiple sets of these prototypes along an arch collectively conceptualize a reciprocal bridge³⁰. However, since this reciprocal configuration remains theoretical and conceptual, the nodes, consisting of misaligned components, are configured only to accommodate binding connections.

In Eastern RF development, the node structure has evolved and refined through practical application (Fig. 1d). The configuration is comprised of 3 distinct systems: the first system, the second system, and the vertical system. Both the first and second systems share the same structural role, with components in each system connected by hinges. Similar to the tessere principle, the vertical system is inserted into the spatial gaps created by the intersections of the first and second systems, thereby establishing nodes where the load is transmitted from one system through the vertical components and further

reinforced by the bending moments of the components in the other system³¹ (Fig. 2a).

However, as the vertical system has to penetrate multiple frame units (comprising the first and second systems) to transmit forces to the global frame, the traditional RF system is limited to accommodate only unidirectional arches³². Drawing inspiration from the force transmission principle of the traditional configuration “tessere il pont,” this study derived an RF configuration adaptable to bidirectional surfaces. This innovative approach reconfigured the vertical component into a component set that incorporates the first and second RF systems, thus extending the adaptability to high curvatures in both surface directions (Fig. 2b). Consequently, this configuration not only expanded the adaptability of the traditional RF system to freeform surfaces, but also retained the inherent redundancy—the reciprocal principle was traditionally conceived as a means of structural reinforcement³³ (compared to trusses, the interlaced connections of components in RF systems present efficiencies in lower space occupancy and increased flexibility in accommodating versatile surface forms).

In the reciprocal prototype of the configuration, the vertical systems along one axis consist of the reciprocal components along the other axis. This principle ensures that the force transmission is equally decomposed and shared by the components along the x and y axes, especially in an orthogonal global configuration. Specifically, the nodes in the first system along the x -axis are supported by corresponding nodes in the first system along the y -axis. However, since the nodes are hinged, the structure remains unstable. The node robustness is achieved when the components of the second system, along both axes, provide support sequentially through their bending moments. Therefore, this configuration not only offers support to the hinged nodes above, but also contributes additional redundancy to the structure.

Nevertheless, as the 4 systems belonging to the two axes need to converge at a single junction, this configuration could induce torsional stresses during force transmission if the systems along the same axis were placed side by side (Fig. 2c), as presented in the traditional configuration. Therefore, the configuration employed an overlapping arrangement of components within the same axis, which makes force transmission more efficient and reduces the frame’s complexity. However, this design approach inevitably increased the complexity at the node intersections between components, thereby enhancing the challenges associated with fabrication^{34,35}. Strategies to mitigate the fabrication challenges will be discussed in detailed the section “Automated Fabrication System of the Configuration”.

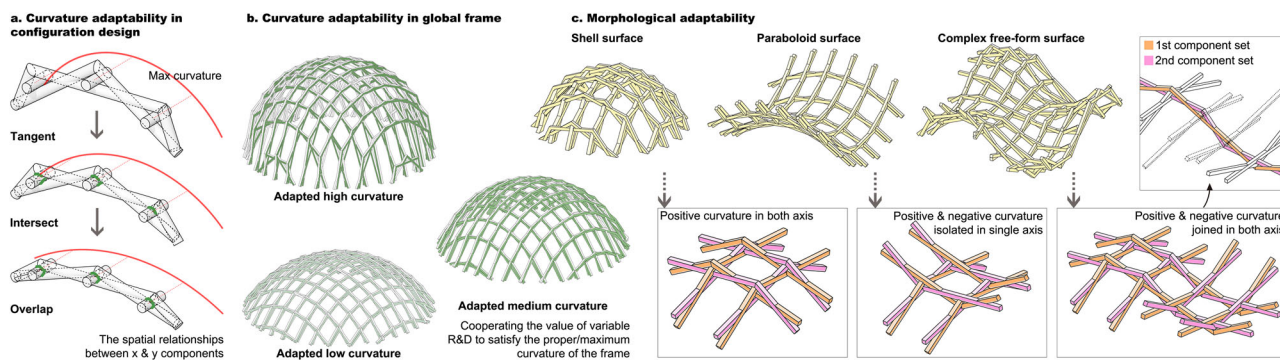


Fig. 3 | Reciprocal frame(RF) prototype morphological adaptability.

a Curvature adaptability of the RF configuration. Considering a typical node-prototype in the traditional configuration as an example. The curvature is maximized when the component in the vertical system is tangent to components in the adjacent first and second systems, and is minimized when the gap between the first and second systems completely disappears. **b** The global forms within the

adaptable curvature range exemplified by a regular shell surface. **c** Morphological adaptability of the RF configuration. The configuration can adapt to various surface morphologies, such as shell surfaces, paraboloid surfaces, and free-form surfaces (variations in positive and negative curvature), based on flexible configurations of node-level formations.

Essentially, in light of the prevalent use of polygonal configurations in contemporary RF systems, this research critically examined the efficiency of orthogonal configurations in traditional RF system during the conceptualization stage. In specific, this study introduced structural topology optimization (TOC algorithm) from a macro-framework perspective to delineate the optimal angular relationship between the systems along the x and y axes in the RF configuration (Fig. 2d, see Supplementary File Table 7 for the TOC algorithm). Based on the Isogeometric Analysis-Based Boundary Penalty Method (IGA-BP)³⁶, this research optimized shell surfaces with varying arch heights³⁷, incorporating Reissner-Mindlin theory to account for shear deformation effects. The base of the shell structure was defined as fixed supports, subjected to approximately uniform-distributed vertical loads. Constraint functions were defined to reduce the structural volume by 50% and 25%, relative to an initially full-material design domain, prioritizing the objective function that maximizes structural stiffness and minimizes static compliance. Optimization results for two arch heights under varied constraint conditions highlighted that an orthogonal arrangement significantly enhances force transmission efficiency within structural engineering context. Consequently, a 90-degree rotation was applied between Fig. 2a, b to achieve an orthogonal arrangement of structural components. Furthermore, the analysis underscored that an orthogonal structural system is economically advantageous, offering greater cost-effectiveness and broader applicability in practical engineering scenarios³⁸.

Morphological generation of the RF configuration

This section presents a parametric morphological generation (PMG) algorithm designed to define the morphology of the configuration, based on the previously discussed design principles. (All algorithms developed in this study have been systematically summarized and are presented in Table 7 of the Supplementary File.)

The PMG algorithm facilitated interdisciplinary collaboration by quantitatively analyzing the impact of design parameter changes on both architectural form and structural performance. Implemented on the parametric programming platform Grasshopper (GH), the PMG algorithm can generate the global framework of the configuration by inputting 3 primary sets of configurational parameters: the target surface morphology, sectional radii of components along the x and y axes (R_x, R_y), and distances between individual frame units along the x and y axes (D_x, D_y). This methodology not only equips architects and structural engineers with an intuitive reference for design decisions during the conceptual phase but also lays down a versatile and targeted parametric foundation for the subsequent structural validation,

optimization, and construction (see details in Supplementary File Fig. 2).

The PMG algorithm introduced formulas that describe the relationship between configurational parameters and the resulting maximum curvature, thus enabling quantitative exploration of the morphological adaptability boundaries of the configuration. Notably, circular cross-sections were used as prototypes for the components, where the distance from the edges to the centroid remains the same. This consideration aids in simplifying the calculation of the relative positional relationships (intersecting, tangential, or separated) between components along the x and y axes. In addition, while the PMG algorithm defaults to a circular section for preliminary calculations, it allows for adaptation to specific requirements. For instance, square sections are employed in structural simulation and fabrication phases, due to the common application in engineering practices. In order to validate force transmission and alteration, the vertical system along either the x or y axis must be at least tangential to each component along the opposing axis. As shown in Fig. 3a, the configuration enables the components of the x and y axes to interlace or fully overlap by milling their cross-sections, thereby enhancing the overall curvature adaptability of the global frame.

Furthermore, the maximum curvature fitting in the configuration principle is derived from the tangential positioning of between the vertical components and components in the first and second system (Fig. 3a). In this context, the configurational parameters influencing curvature fitting include D (comprising D_x and D_y) and R (comprising R_x and R_y). D dictates the latitudinal extension of the curve, while R , given the tangential principle between components, limits the longitudinal extension of the curve.

Figure 3b demonstrates the curvature adaptability of the global frame of the configuration generated by the PMG algorithm, employing a shell surface with a 15 m span as a case prototype. The figure illustrates the influence of configurational parameters D and R on curvature variation. Notably, the example showcasing the highest curvature in the figure (span-to-rise ratio of 1.2) represents a curvature range that has not yet been achieved by contemporary RF configurations. Above all, this study derived the quantitative relationships between the maximum allowable curvature C_{max} and the variables D, R (including variables along both axes). Further details are provided in the Supplementary File Fig. 3.

Moreover, in terms of architectural morphology design, the PMG algorithm fits freeform surfaces commonly utilized in architectural engineering, including classical spherical surfaces, hyperbolic paraboloids characterized by positive curvature in one direction and

a. Multi-objective optimization indicators

Multi-objective evaluation indicators	Architectural perspective indicators			Structural perspective indicators					
indicators	M	V	α_1	α_2	β_1	β_2	T_f	F_f	F_n
Unit	m^3	-	-	-	-	-	mm	KN	KN

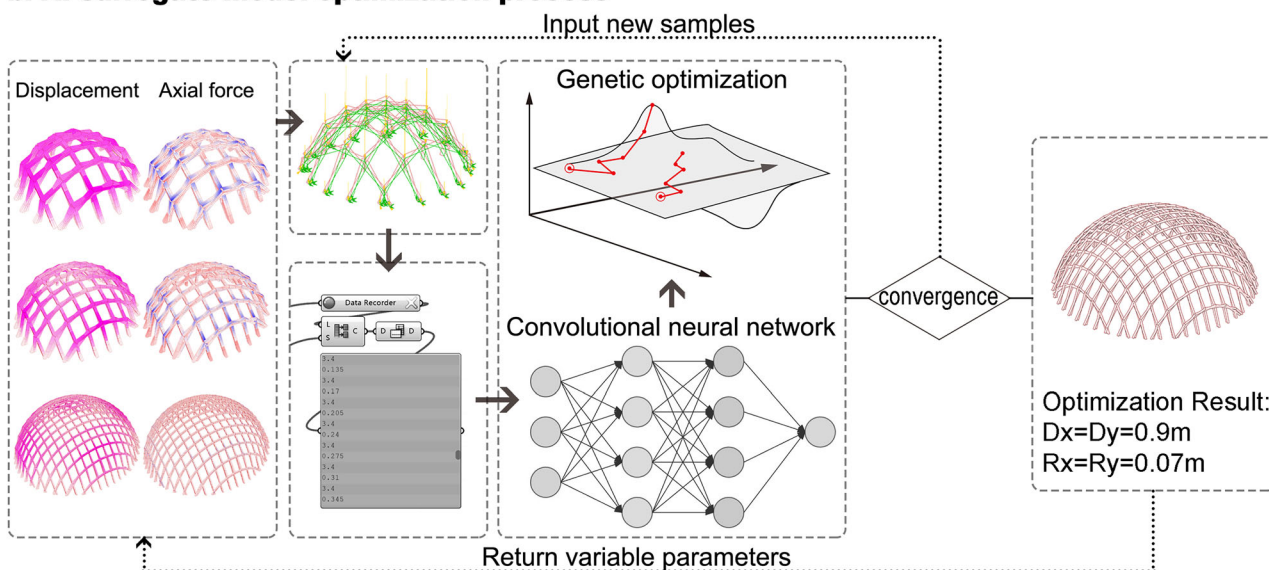
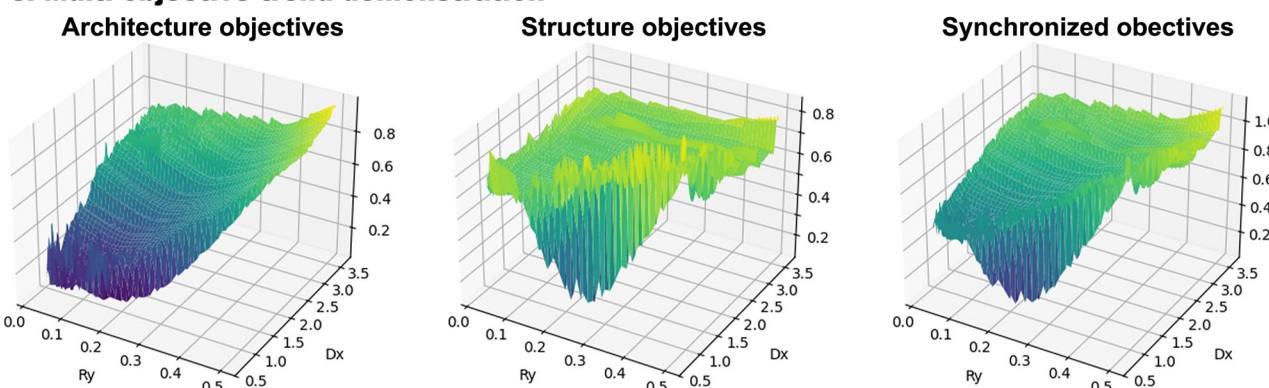
b. AI surrogate model optimization process**c. Multi-objective trend demonstration**

Fig. 4 | AI surrogate mode optimization. **a** Multi-objective indicator. This study establishes a comprehensive evaluation system for the configuration, incorporating architectural evaluation indicators, such as space occupancy(V) and material usage(M) and structural indicators, including structural displacement (T_f), tensile force (F_f), and compressive force (F_c). **b** AI surrogate model optimization process. Starting with a hemispherical with a 15 m diameter, the structural performance of the configuration is analyzed under varying design variables (section radii R and

frame distances D) based on FEA. Surrogate model analyzes trends between variables and disciplinary objectives and establishes approximate functional relationships, based on AI deep learning. **c** Multi-objective trend variations with variables (Ry represents sectional radii of components along the y axis, and Dx represents the distance between individual frame units along the x axis). The z-axis represents the weighted normalized objectives, where a smaller value indicates higher efficiency.

negative in another, and special surfaces exhibiting both positive and negative curvature variations in two directions³⁹ (Fig. 3c). At the node level, the configuration shown in Fig. 3c can be inverted to accommodate surfaces with negative curvature. This is achieved by applying a load to the ends of hinged components, thereby inducing an upward force tendency at the intersections and inversely leveraging the bending moments of the reinforcing components to enhance global stability. Therefore, the node intersection fitting negative curvature is unsuitable for directly bearing loads - when the downward force acts on the hinged nodes, the components above, which are supposed to

provide bending moments, only transmit the force rather than produce direct support and reinforcement. Consequently, the configuration is generally inadvisable for bowl-shaped forms that consist solely of negative curvature, which are also relatively rare in architectural engineering applications⁴⁰. By integrating the configuration prototype with its inverted form, the configuration is capable of adapting to surfaces with both positive and negative curvature in each direction. Specifically, this involves overlapping the first systems of both configurations at the junction and connecting the second systems (Fig. 3c). See the configuration details in Supplementary File Fig. 4).

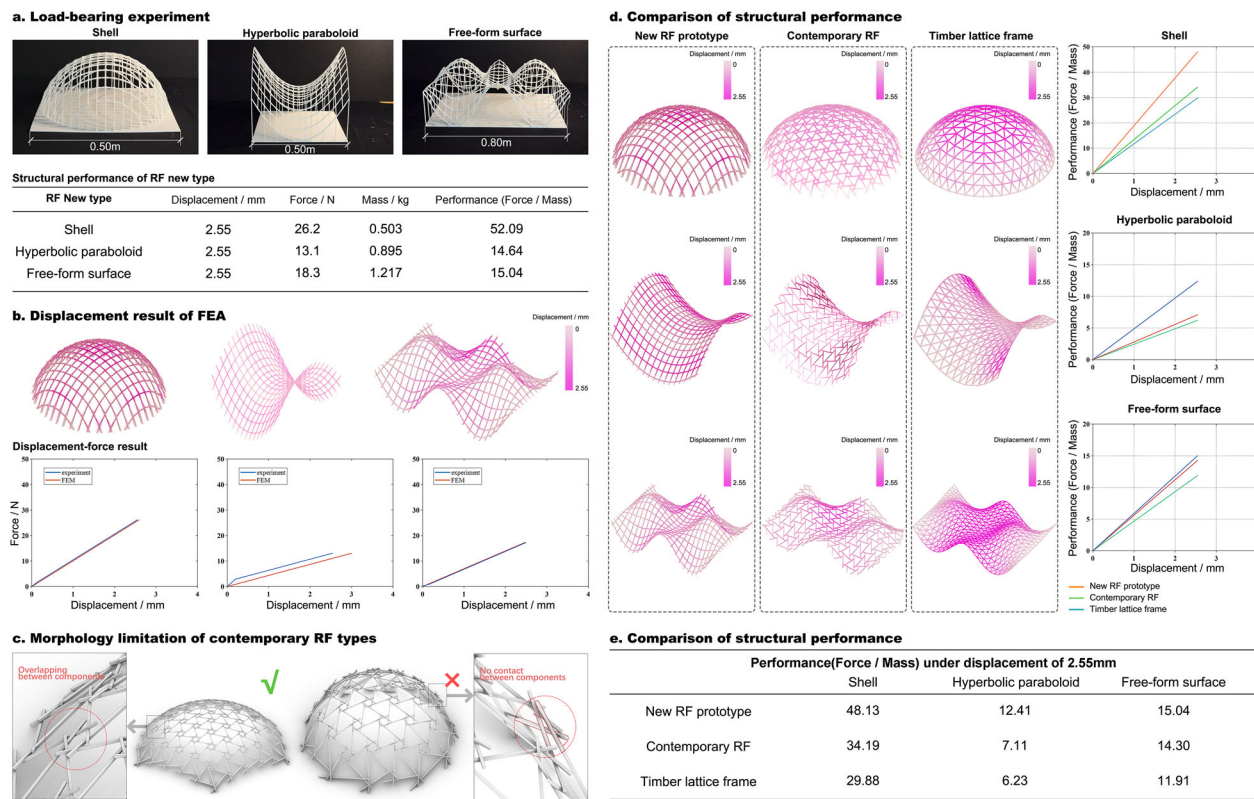


Fig. 5 | Structural advantages of the RF configuration over traditional configurations under different shapes. **a** Under a central top displacement of 2.55 mm, the shell, hyperbolic paraboloid, and the free-form surface sustained concentrated loads of 26.2 N, 13.1 N, and 18.3 N, respectively. **b** The comparison between finite element simulations and load-bearing tests validates the accuracy of the finite element analysis. **c** The configuration of components in contemporary RF systems reveals limitations in accommodating large curvatures. **d, e** Comparison of

structural performance among 3 types of timber frames. With the same maximum displacement, the structural performance of the RF prototype in the shell form is 1.41 times better than that of contemporary RF and 1.61 times that of the timber lattice frame. The RF prototype outperforms the other two contemporary systems by approximately twofold in the hyperbolic paraboloid. In the free-form surface, the RF prototype performs 1.05 and 1.26 times over the contemporary RF and timber lattice frame, respectively.

In summary, the configuration can accommodate any variation of positive and negative curvature in two directions within the architectural engineering realm, demonstrating high adaptability to free-form surfaces. It thereby significantly extends beyond the quantitative curvature adaptability of contemporary RF systems.

Interdisciplinary performance evaluation

As previously mentioned, the configuration exhibits exceptional curvature adaptability. When numerous components are “reciprocal” to fit the global morphology, adjustments in the scale of local elements or even the overall shape not only affect the architectural expression of the configuration but also have an immediate impact on its structural performance.

Consequently, this study developed a set of indicators to create a comprehensive evaluation system, analyzing the quantitative effects of design parameter variations on architectural and structural performance from an interdisciplinary perspective (Fig. 4a). It is worth mentioning that this indicator system is primarily developed for preliminary evaluations during the early design phase. The composition of the indicators is flexible and can be tailored to meet the specific needs of varying design scenarios. For example, a weighting factor can be incorporated into the composite metric to linearly combine multiple sub-objectives (such as stiffness and material usage). By assigning different weights to material consumption, redundancy can be adjusted, allowing a more flexible balance between stiffness and material usage and thus accommodating design priorities such as ‘maximizing stiffness’ or ‘minimizing material usage’.

From a structural perspective, the structural performance of the RF configuration was verified by a parametric structural simulation (PSS) algorithm (based on finite element analysis FEA, see Supplementary Table 2 for experimental setup details) to assess its structural efficiency and load-bearing capacity under various configurational parameters. To simulate real-world conditions, the PSS algorithm incorporated 4 types of loads: self-weight, dead load, live load, and wind load. The configuration also demonstrates adaptability and robustness under seismic load scenarios (see Supplementary Fig. 15 for detailed simulation verification). Larch wood, selected for its cost-effective and widespread application, served as a material prototype for the frame. Importantly, in response to the section loss due to the interlacing of components in Fig. 2c, the PSS algorithm performed meticulous calculations at the sectional level. The accuracy of the load-bearing capacity of the frame was ensured by this detailed analysis of load distribution across various sectional loss areas and the relative positions of multiple components at one node (see details in supplementary file Fig. 5).

This study selected 3 evaluation indicators based on the fundamental requirements outlined in the standard for preliminary design (referring to JGJ 7-2010 “Technical Specification for space frame structures”):

- (1) Structural Displacement (Tf): The maximum displacement of the entire structure.
- (2) Tensile Force (Ft): the maximum tensile force experienced by any member within the structure.

(3) Compressive Force (Fn): The maximum compressive force experienced by any member within the structure.

From an architectural perspective, architects are tasked with a comprehensive balance and manage of space, materials, and morphological composition in the initial design phase⁴¹. Thus, this study established the following evaluation indicators:

- (1) Space – Space Occupancy Ratio of Frame (V): This indicator quantifies the interference of the framework with space design, epitomizing the efficiency of space utilization. A lower efficiency value indicates minimal interference with space design, presenting higher functional utility of the enclosed/100 spaces.
- (2) Materials – Material Usage (M): This indicator describes the total materials consumption required to construct a framework of a certain scale and morphology, which directly affects construction costs and sustainability. It serves as a crucial metric for “material conservation” in the evaluation of contemporary green building⁴²
- (1) Morphological Composition – Configurational Efficiency (α_1 , α_2 , β_1 , β_2): This set of indicators can assess the efficiency of employing components with a maximum length (Q) or a cross-sectional area (A) to construct a global frame achieving a maximum span (L) or curvature (C). Consistency in the frame scale with lower efficiency values indicates a reduced scale of materials used. This underscores the RF characteristic of “small material, large span”, highlighting its diminished dependency on large-scale timber resources. The relationships are articulated as follows:

$$\alpha_1 = Q/L \quad (1)$$

$$\alpha_2 = A/L \quad (2)$$

$$\beta_1 = Q/C \quad (3)$$

$$\beta_2 = A/C \quad (4)$$

Quantitative design-guide via multi-objective optimization

Although PMG and PSS algorithms provide precise performance analyses under specific parameters, the trending calculation of linking configuration parameters to evaluation indicators (objectives) is highly time-consuming due to its numerical intensity and geometric complexity. Consequently, this study introduced an AI surrogate-based multi-objective optimization approach^{43,44}.

This approach incorporates an interdisciplinary evaluation system for the RF configuration, encompassing both architectural and structural disciplines. It efficiently captures the overall quantitative relationships between design variables and performance indicators, thereby offering valuable guidance to architects and engineers during the initial design stage (Fig. 4b). From an operational perspective, users only need to input the target surface morphology along with allowable ranges of (Rx, Ry) and (Dx, Dy), export multiple parametric combinations to an Excel file within the Grasshopper environment, and then import the file into the AI-SMO algorithm module to automatically obtain the optimal design parameters. This workflow is highly accessible, requires no complex operations, and can be easily learned and applied by regular design practitioners.

Therefore, this work simulated the corresponding objective values for 1500 sets of variable combinations via a sampling method (see Supplementary File Table 4 for the data derived from PMG and PSS algorithm), based on a 15 m span hemisphere as a prototype (as shown in Fig. 4b left). Furthermore, a suite of surrogate models was

developed to approximate functional relationships, effectively replacing the FEA “black box”. This method allows for a more direct analysis of the overall quantitative trends between variables and objectives. The findings are as follows (Fig. 4c):

- (1) From the architectural perspective, the observed trend reveals a pronounced trough from larger to smaller D and R values. This indicates that smaller D and R values significantly enhance the overall efficiency in architectural form, streamlining the use of space and improving aesthetic integration.
- (2) From the structural perspective, all variable values depicted conform to the necessary structural stability requirements. The impact of larger D values on structural performance is generally minimal, with only slight fluctuations observed. However, as D values approach their minimal threshold, there is a notable enhancement in structural performance. Specifically, with smaller D values, the performance of R values tends to be lower at both extremes and higher in the middle, suggesting a bell-shaped performance curve.
- (3) From a collaborative perspective, there is a clear shift from configurations with large D and R values, which exhibit low efficiency, to those with small D and R values, which demonstrate high efficiency. However, due to the influence of structural considerations, the optimal R value is not at the extremes but rather found centrally. The predicted optimal solution is $Dx = Dy = 0.9$ m, and $Rx = Ry = 0.07$ m.

In addition, given that a centrally symmetric hemisphere serves as the surface prototype in this study, the influence of Rx and Ry on the objectives are mirrored, a pattern also applicable to D values. Therefore, only the variables Dx and Ry are shown in Fig. 4c (the optimization trend for each objective is provided in the supplementary file Fig. 6). For more intricate surface conditions encountered in practical engineering applications, a targeted analysis of the quantitative impacts of all configurational parameters on each objective will be required, applying AI surrogate optimization. However, such scenarios extend beyond the scope of the prototype employed in this study.

Mechanical experiment with various conditions

Based on the optimal solution of a classic hemisphere with a span of 15 m (where $D = 0.9$ m and $R = 0.07$ m), a 1:30 scale physical model was constructed using a 3D printing machine. In addition, this section includes the construction of typical mathematical surfaces, such as hyperbolic-paraboloid and free-form surfaces (under the same design parameters) to demonstrate the practical adaptability and generality of the configuration. The maximum curvature of these surfaces is 0.267.

Consequently, compression tests were conducted on 3 types of morphologies with dimensions of 500 mm in span to evaluate its load-bearing capacity. As depicted in Fig. 5A, the experimental setup secured the bottom of the prototype to prevent displacement along the z-axis, while a concentrated incremental load was administered at the central top of the prototype via an actuator. The displacement at this point was instantaneously recorded (see Fig. 7 in the supplementary file for details of the experiment).

Among the three forms, the shell frame exhibited a displacement of 2.55 mm under a concentrated load of 26.2 N. At the same displacement, the hyperbolic-paraboloid and free-form frame were subjected to concentrated loads of 13.1 N and 18.3 N, respectively. Given the differences in mass among the three, their structural performance per unit mass was 52.09 (shell), 14.64 (hyperbolic-paraboloid), and 15.04 (free-form) (Fig. 5a). The high performance of the shell frame is attributed to its arch-like surface, which better facilitates force transmission, and the relatively stable support points of the shell model.

Figure 5b displays the simulated stress distribution under this load, derived from a static loading FEA through the PSS algorithm. The

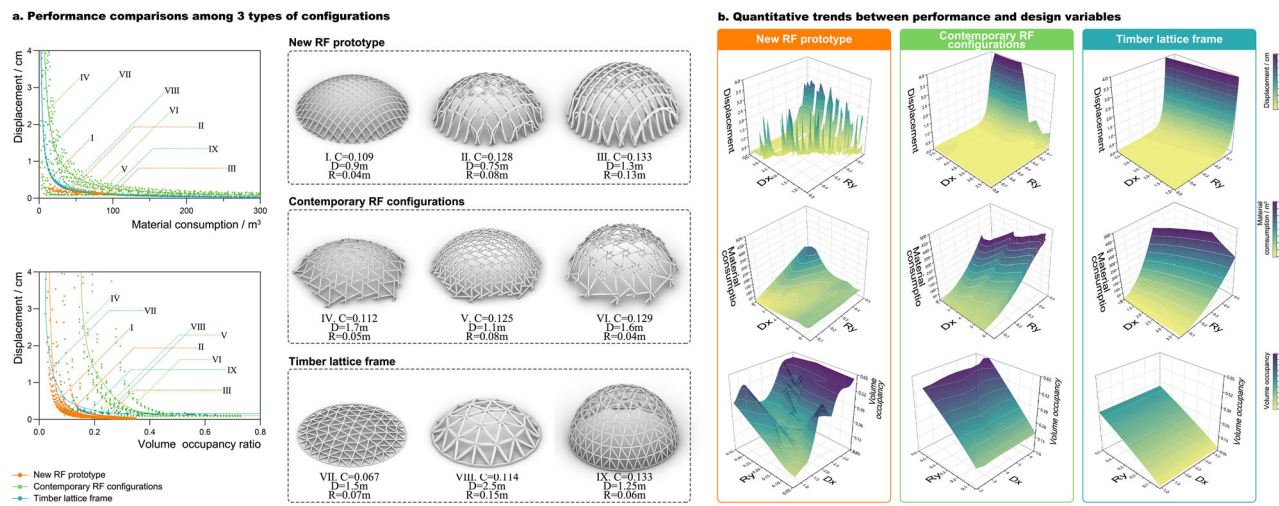


Fig. 6 | Global comparisons among 3 configurations in large sample space.

a With equivalent material usage, the RF prototype demonstrates high structural performance over the contemporary RF configuration and holds a modest advantage over the timber lattice frame. When occupying the same spatial volume, its structural displacement is markedly lower than that of the contemporary RF configuration and the timber lattice frame. Nine frames with varying configurations and design parameters (frame distance D, component cross-sectional radii R and fitted curvature C) are presented to clarify the comparison, labeled I–IX in sequence. The

corresponding I–IX symbols are also marked in Fig. a to indicate the data points representing each frame. b Quantitative trends between performance and design variables offer architects intuitive guidance for initial design decisions (Ry represents sectional radii of components along the y axis, and Dx represents distance between individual frame units along the x axis). The RF prototype demonstrates high structural performance (average displacement reduced by 24.37%) and greater material efficiency (average material usage reduced by 33.13%).

parameters used in the model were consistent with those of the experimental prototype. The comparison of force-displacement curves obtained from simulations and experiments for the three forms reveals a close correlation, with deviations ranging from 3% to 12%. This discrepancy is attributed to material gaps inherent to 3D printing, which resulted in a reduced initial elastic modulus and a steeper initial slope in the experimental curve, deviations that were not considered in the PSS algorithm. However, the slopes of both curves aligned well after material compaction, confirming the feasibility of the PSS algorithm for assessing concentrated load scenarios and its suitability for simulation experiments in this configurational framework.

Furthermore, when comparing the structural performance between the RF configuration and contemporary RF through experimental trials, it becomes evident that contemporary configurations cannot accommodate the required curvature: the excessive curvature prevents effective contact and force transfer between components (Fig. 5c). Contemporary RF can only accommodate a maximum curvature of 0.117 in the context of a 15 m span, further demonstrating the morphological adaptability of the configuration (the quantitative curvature boundary of the configuration is demonstrated in Supplementary Fig. 3). Thus, compared to the existing RF, the RF configuration exhibits curvature adaptability, thereby expanding its potential in engineering applications from a morphological perspective.

To compare the configuration with contemporary RF and mainstream timber lattice frames, the maximum curvature of the three surfaces adapted by the configuration was reduced from 0.267 (as shown in Fig. 5a, b) to 0.117. The nine sets of simulated design parameters (excluding maximum curvature) in Fig. 5d are consistent with those in Fig. 5a. The results indicate that, with structural displacements of 2.55 mm, the configuration demonstrates a structural performance that is 1.41 times greater than that of contemporary RF and 1.61 times greater than that of timber lattice frame for the shell context. For the hyperbolic-paraboloid surface, the configuration's structural performance is approximately twice that of both contemporary methods. The free-form surface shows similar results, with the configuration's performance surpassing contemporary RF and timber lattice frame by factors of 1.05 and 1.26, respectively. In summary, the configuration

consistently outperforms the two contemporary methods in structural performance under the same morphological conditions (Fig. 5e).

Comprehensive comparisons with alternative configurations

In the previous section, we compared the structural performance of three different configurations under a specific set of design parameters. This section will further explore the macroscopic trends between design parameters and structural performance via statistical analysis. In addition, from an interdisciplinary perspective, we argue that structural performance is only one aspect of evaluation. To provide a more comprehensive assessment, material usage and space occupancy are introduced as additional indicators from an architectural perspective.

However, the results shown in Fig. 5d reveal significant variations in structural performance among different surface forms. Grouping multiple global forms for statistical analysis may affect the goodness of fit and consequently impact the accuracy of trend exploration. Therefore, this section introduces the classic and simplest shell form as a representative.

We simulated 3000 performance datasets for the configurations that meet basic structural specifications, varying design parameters (frame distances D, component section radii R, and surface max curvature C), based on the material properties of pine wood. Furthermore, we developed morphological generation and structural simulation algorithms for contemporary RF configurations and timber lattice frames (see Supplementary Table 3 for data collection method). Similarly, 3000 datasets for the 2 existing configurations were generated to conduct a quantitative comparison of macroscopic trends with the configuration (details are provided in Supplementary Fig. 8 and Tables 5, 6, see Supplementary Table 7 for more information on developed algorithms in this paper).

Figure 6a illustrates the distribution trends of structural performance differences among the three configurations under identical material usage and space occupancy conditions. The results are as follows:

- (1) Different combinations of design parameters directly impact material usage and space occupancy, which in turn affect the

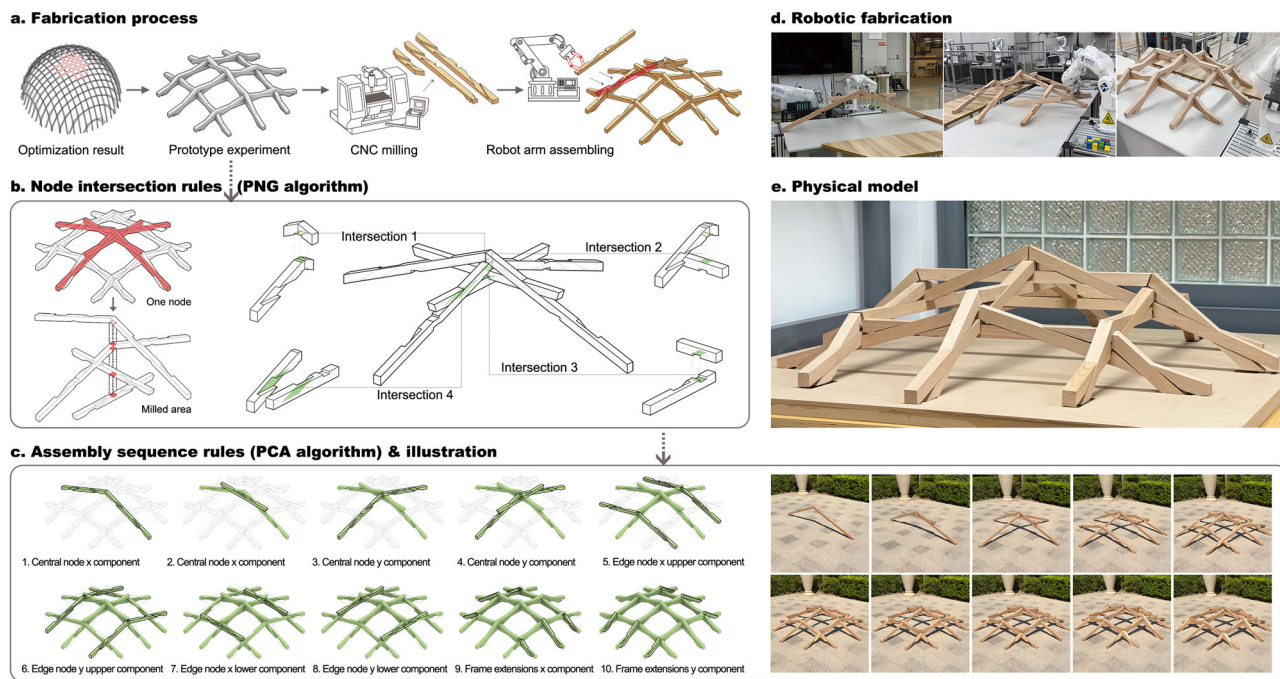


Fig. 7 | Fabrication of the Prototype. **a** Fabrication Process. The process began with parametric design and node generation in Grasshopper (GH), followed by CNC cutting of the components. Robotic arms then automatically assembled the pieces according to a predetermined sequence. **b** Node Intersection rules. Each node in the configuration integrates 4 systems, intersecting horizontally and vertically to form 4 distinct junction types, each requiring unique cutting methods. **c** Assembly Sequence. The assembly rules were defined as center-outward in the planar direction and x-axis to y-axis in the sectional direction. **d** Robotic Fabrication. Due

to the complexity of node intersections, digital twin technology was employed to control robotic arms for automated assembly, with human-robot collaboration for oversight. The scaled model demonstrated strong load-bearing capacity and efficient assembly (23 min) and disassembly (5 min) with human-robot collaboration. **e** Configuration Disassembly. The design allows rapid disassembly and replacement of components. The frame maintains significant load-bearing capacity even with some components missing, demonstrating structural redundancy.

overall structural displacement. In general, under conditions of equivalent material usage (and thus structural mass), the configuration's structural performance is, on average, approximately 32.26% higher than that of contemporary RF configurations but only about 8.92% higher than that of timber lattice configurations. Specifically, when the material usage exceeds 100 m^3 or 50,000 kg, the structural displacement of the configuration and timber lattice approaches similar values. In addition, the configuration can save up to approximately 37 m^3 of material under the same structural performance. Despite requiring a higher number of components due to its reinforcement principle, the configuration features significantly smaller cross-sections, ultimately leading to a reduction in overall material consumption.

- (2) When the space occupancies are equivalent, the structural displacement of the configuration is, on average, 79.22% lower than that of contemporary RF, but only 11.75% lower than that of timber lattice frames. Specifically, within the allowable maximum displacement range, the minimum space occupancy of the configuration is 5.4%, compared to a lower threshold of 3.3% for timber lattice frames: since the configuration requires intersecting two independent systems along an axis. Although this results in greater space occupation, it provides structural redundancy and additional stability. Moreover, for the same structural performance, the configuration can reduce space occupancy by up to 18.34%.
- (3) The configuration also has certain limitations. As shown in the comprehensive performance analysis of various architectural and structural indicators in Supplementary Fig. 13, one drawback lies in its slightly lower configurational efficiency (spanning

by a smaller component) compared to the conventional timber lattice frame. Specifically, it requires relatively longer members to achieve the same stiffness. This is because, in order to enhance structural redundancy, the members in the configuration are longer for the same span. However, this trade-off results in improved resistance to failure and greater structural ductility due to the increased redundancy.

Furthermore, since the structural space occupancy and material usage presented in Fig. 6a are depicted as ranges that encompass various morphological performances stemming from different combinations of RF configurational parameters, it is crucial to correlate these ranges with specific design parameters. This correlation facilitates designers in integrating architectural and structural considerations during the conceptual design phase. Therefore, Fig. 6b illustrates the macroscopic trends performance indicators (structural displacement, structural space occupancy, material usage) and configuration parameters (frame spacing D, component cross-section R) for the 3 configurations. The results are as follows:

- (1) Structural Displacement: Compared to the other 2 configurations, the configuration achieves an average reduction of 24.37% in structural displacement, indicating high structural performance. The relationship between structural performance and design parameters reveals a distinct improvement as both R and D values increase, while in existing configurations, only the R value directly impacts structural performance.
- (2) Material Usage: The configuration demonstrates an average reduction of 33.13% in material usage compared to contemporary configurations, reflecting higher material efficiency.

The material usage in the configuration is also notably sensitive to the coordination of D and R values. As depicted in Fig. 6b, architects have the flexibility to select different design variables to achieve equivalent material usage. This variability allows for different structural forms and performances, enabling precise selections tailored to specific engineering requirements.

(3) Spatial Occupancy: Due to the presence of two independent systems in each arch of the configuration, its spatial occupancy varies more complexly with design parameters and is locally higher than that of existing configurations. In contrast to the contemporary configuration, the configuration demonstrates a pronounced impact of D values on its space occupancy. Specifically, variations in D values in the configuration more directly affect the angles between connecting components compared to the planar-like units in the contemporary configuration. This variation influences the structure's space occupancy and its interaction with the created space. Consequently, the adaptable coordination of configurational parameters in the RF system can significantly enhance space utilization efficiency.

Automated fabrication system of the RF configuration

To enhance the constructability of the proposed RF configuration in real-world construction, this study incorporates constructability-oriented node design constraints into the parametric design workflow. Inspired by the component standardization approach proposed by Cucuzza^{21,22}, we minimize the variety of cross-sections and node types, thereby simplifying the preparation process for construction. In addition, the connection methods between components are constrained to planar or near-coplanar configurations to avoid complex spatial joints, thus improving assembly convenience and fabrication accuracy. As a result, the design process extends beyond structural performance and morphological expression to address efficiency and sustainability throughout the entire digital construction workflow from the outset, providing both theoretical and technical support for the practical realization of complex timber structures.

Moreover, in response to the challenges associated with preserving a uniform structural hierarchy in RF systems, this study introduced a parametric construction methodology that simplified complex and hard-to-recognize assembly sequences into algorithmic rules. The objective is to demonstrate the feasibility of a digital design and construction workflow, thereby validating the configuration's capabilities for automated and rapid deployment.

This methodology enhances the construction process through human-robot collaboration. The specific construction principles are as follows: managing parametric node connection designs on the GH platform to ensure assembly feasibility, generating BTL files (Biesse Tool List, a file format for CNC fabrication) for CNC machining, establishing parametric rules for assembly sequences, and enabling robotic arms to assemble the processed components based on digital twin technology (Fig. 7a).

This section selected 9 central nodes in the 15 m hemispherical morphology discussed in the optimization section. This 9-nodes physical model was constructed at a 1:2 ratio to thoroughly demonstrate the construction and assembly details of the configuration. Consequently, the scaled prototype model was fabricated with a 0.45 m distance between individual frame units, a 3.5 cm component diameter (side length of the square cross-section), and a 1.8 m span with a total projected area of approximately 2.54 m². (See the compression tests of this local model in Supplementary File Fig. 9).

Node connection design. This section delved into the node connection design of the configuration, specifically tailored for surfaces exhibiting continuously variable curvature. Due to varying angles of component intersections, node connections in the configuration differ in size and sectional losses. The interconnection design at each node

was managed by the parametric node generation (PNG) algorithm, enabling precise calculations of the cutting positions and dimensions of components (the PNG algorithm also supports targeted FEA of components in the PSS algorithm of the configuration).

Given the intricate nature of node interconnections and the variability in sectional losses, the application of CNC manufacturing substantially improved processing efficiency, ensures precision, and reduced production costs^{45,46}. Typically, each node in the configuration includes 4 intersections formed by 4 systems along the x and y axes (Fig. 7b):

Intersection 1: This intersection consists of 4 components from the first systems along the x and y axes. The PNG algorithm treats the components along each axis as a coherent unit, forming a plane at the interlacing of their outer surfaces and cutting the components of both axes based on this plane.

Intersection 2: This intersection consists of 2 components from the first system along the x-axis and one component from the second system along the y-axis. To preserve the material integrity of the reinforcing components, cuts are performed solely on the components of the first system along the x-axis.

Intersection 3: This intersection consists of 2 components from the second system along both axes. Since both components are for reinforcing, a cutting plane was established at the midpoint of each interlaced edge. This method ensures that the volumes are divided equally, thereby minimizing the loss of bending moments in any single component.

Intersection 4: When the two systems along a single axis intersect, the milling of the components follows the equal division principle in Intersection 3, with the cutting plane shifting to z-axis.

Robotic arm assembly. In light of the consolidated configurational principles, this study defined the basic assembly rules for components from the center to the periphery in the planar direction and from the x-axis to the y-axis in the sectional direction via the Robot plugin on the GH platform (Fig. 7c).

The assembly process commences at the central node of the frame. The process starts with installing the components of the first system along the x-axis (at the top of the node), followed by the components of the second system along the x-axis (beneath the aforementioned components). Subsequently, a similar sequence is executed for the y-axis systems, thereby completing the assembly of the central node.

From the central node, the corresponding components of the two systems along the y-axis are installed on both sides of the x-axis direction, proceeding from top to bottom. Simultaneously, components along the x-axis are installed on both sides of the y-axis direction from the central node. Finally, the components at the ends of each frame unit are installed. They are integral to the complete assembly process for expanding additional nodes. This model demonstrated the assembly process for 9 nodes, significantly fewer than typically encountered in actual engineering applications. Nonetheless, based on this assembly experiment, the assembly logic—from the center to the periphery for node positions and from top to bottom for components along both axes—has proven effective.

Upon establishing the parametric rules for assembly sequence, digital twin technology was introduced to transmit the simulated assembly process to robotic arms for automated construction. However, due to the various interlacing directions of components at the nodes in the configuration, it is challenging for the uniaxial forces produced by robotic arms to independently install the components at the target locations. Consequently, the entire robotic assembly process must be supervised and supplemented by human collaboration, functioning as an “agent” (Fig. 7d). In addition, Fig. 7E underscores the advantages of component disassembly and renewability in the configuration: upon removal of any component, the framework remains

intact and retains its load-bearing capacity. This demonstrates the structural redundancy that sets it apart from contemporary RF systems.

Furthermore, in contemporary RF systems, the polygonal component arrangements require complex spatial positioning and advanced 3D manufacturing for robotic construction. It is challenging to avoid errors under current technical conditions^{47,48}. The configuration demonstrates that orthogonal arrangements can effectively address complex engineering challenges. With fewer linear directions in the orthogonal assembly and a limited number of members connected per node, error propagation throughout the structure is reduced, thereby expanding the allowable error range in spatial positioning and 3D fabrication and enhancing the feasibility of automated construction.

In conclusion, based on the arguments presented in the previous two sections, the proposed configuration demonstrates clear advantages in terms of material usage and construction efficiency. Specifically, it achieves a reduction of approximately 33% in material consumption compared to mainstream contemporary timber structural systems, thereby offering lower construction costs. The CNC milling process for this configuration requires only 3 min per element, which is approximately a 90% time saving compared to traditional fabrication methods that typically take 1–1.5 h per element [55]. Moreover, the integration of a digital twin system eliminates errors in assembly and component identification, ensuring a stable and efficient assembly process. Prototype tests of the configuration reveal a high assembly efficiency of approximately 9.1 min per m². In contrast, contemporary timber lattice structures generally require 30–60 min per m² [56], and current RF configurations often exceed one hour per m² [55], highlighting the timeliness of our system. Furthermore, the configuration retains a high degree of flexibility even within timber construction systems: thanks to the quantifiable logic governing both joint connections and assembly procedures, disassembly is efficient and adaptable. While traditional structural systems often demand extensive training for construction workers, the human-robot collaborative assembly process significantly reduces this hidden cost as well.

Discussion

Over recent decades, modernism's introduction of industrial materials has significantly propelled global technological advancement^{49,50}. However, it has also contributed to environmental pollution and degradation. This development has revitalized interest in timber structures within the architectural engineering field⁵¹. Given the current scarcity of timber, RF systems present substantial potential for application despite their inherent morphological and structural limitations. The proposed RF configuration design aims to overcome these deficiencies, specifically addressing the lack of structural redundancy and limited adaptability to complex curvatures. To this end, we have made the following efforts:

- (1) proposing a RF configuration design method from a collaborative perspective, which provides a comprehensive parametric platform for architectural and structural design, multi-objective optimization, and automated construction;
- (2) offering quantitative guidance for the initial design of the RF system, based on design variables and target efficiency through interdisciplinary support;
- (3) effectively enhancing the morphological adaptability, providing the missing structural redundancy, reducing space occupancy, and decreasing material usage of contemporary RF systems.

The RF configuration combines the advantages of small-scale components, large spans, modularity, high structural performance, and rapid deployment (simple assembly), exhibiting good scalability and potential application to large-scale structures (see Supplementary

Fig. 14). It can meet diverse engineering and industrial needs with materials of varying performance characteristics. Nevertheless, during practical deployment, further consideration should be given to both the stricter demands for structural stiffness and the potential influences resulting from decreased overall curvature. Furthermore, its exceptional adaptability to curvature offers significant advantages within a broader range of design parameter values, potentially making it the only viable choice in certain contexts. These features enable the configuration to significantly reduce engineering costs in civil engineering while providing flexible, time-efficient, and high-performance solutions with enhanced structural expressiveness. We believe that this innovative construction approach not only challenges the current mainstream concepts of timber structures and RF systems but also has the potential to transform the entire lifecycle of rod structures: from conceptualization and design to optimization, manufacturing, and deployment.

However, this study provides convincing results based on small-scale specimens and numerical models, but has not addressed the potential issue of scale effects. In real engineering applications, the structural components are much larger than those used in the experiments and simulations, which may lead to changes in mechanical response, crack propagation paths, and energy dissipation mechanisms. These factors could influence the overall load-bearing performance and structural robustness. Therefore, future work should involve large-scale specimen tests or on-site experiments to further verify and refine the applicability and reliability of the proposed system.

Methods

IGA-BP Topology optimization method

Isogeometric Analysis-Based Boundary Penalty (IGA-BP) method is an advanced approach that combines isogeometric analysis (IGA) and boundary penalty techniques to optimize structural topology. IGA employs spline-based representations for both geometry and analysis, which are used in computer-aided design. This use of consistent representations avoided the geometric approximation errors often encountered in the traditional FEA method, ensuring more accurate modeling and analysis of complex structures.

The boundary penalty method facilitates the enforcement of constraints in the optimization process by incorporating them into the objective function as penalties. This integration enhances the flexibility and efficiency in finding optimal solutions. This methodology is particularly advantageous for precision-critical applications in engineering, allowing for detailed control over structural responses and efficient handling of complex design conditions.

Multi-objective optimization via AI surrogate models

A convolutional neural network-based AI surrogate model was utilized to identify an input-output functional relationship between configurational parameters and objectives, culminating in the development of a predictive model (Fig. 4b). The surrogate model commenced with data preprocessing, employing methods such as outlier exclusion and normalization to refine inputs. Subsequently, a multi-layer perceptron (MLP) was constructed, featuring several nonlinear hidden layers and utilizing the ReLU nonlinear function for fitting. To prevent overfitting, an early stopping mechanism was integrated into the training process. The resultant model achieved a goodness-of-fit score of 0.996, demonstrating a high level of predictive accuracy.

In addition, acknowledging the necessity of balance for interdisciplinary collaboration, this study assigned equal weights (0.5 each) to 6 architectural indicators and 3 structural indicators. A genetic algorithm was subsequently employed to determine the optimal D and R values that maximize morphological and structural efficiency for specific target surface conditions. Notably, while gradient-based algorithms are prone to falling into local optima during multi-

objective optimization, the genetic algorithm was selected to ensure a globally optimal solution. Although generally less efficient, the genetic algorithm does not incur additional time costs when optimizing simple mathematical models.

Automated construction

Computer numerical control (CNC) manufacturing. Following the PNG algorithm, the experimental prototype was fabricated using a 5-axis CNC machine outfitted with a milling cutter of 4 mm diameter and 4 cm length. The Grasshopper (GH) script, detailing the algorithmic rules, automatically generated BTL files, which were transmitted to the robotic arms. These BTL files govern the milling cutter's movements, processing each groove. The existing BTL library^{52,53}, specifically tailored for wood processing, guaranteed consistent milling outcomes, irrespective of changes in the cutting tool.

Assembly

The assembly phase utilized two Genertec i5-A3 robotic arms (Max. Load 4 kg), each equipped with a pneumatic gripper. Especially during the initial phase of assembly, the rods were unable to maintain stability independently when manipulated by a single robot. Thus, the parametric component assembly (PCA) algorithm organized them into odd and even groups according to the predetermined sequence (Fig. 7c), enabling coordinated, simultaneous assembly by the two robotic arms. Furthermore, a “work object” (symbolizing the log's (X, Y, Z) reference system) and an “axis configuration” were established for the robots, facilitating effective evasion maneuvers as the arms transport rods to the target.

Regarding human-robot collaboration, each component was marked with a specific serial number during the CNC milling stage. The supervisor positioned these components at predefined spots based on their serial numbers (sorted into odd and even groups), simplifying the robotic arm's retrieval tasks. Each placement of a component by the robotic arm constituted a “task,” involving precise maneuvers of the gripper (defined by the Tool Center Point) to designated positions within the workspace. Supervisors verified the successful assembly of each component after every task and before proceeding to the next. In cases where a component failed to align correctly due to spatial discrepancies or other issues, immediate collaborative intervention by the supervisor was necessitated.

Determination of material performance for experiment

The Experimental prototype of the configuration was produced using 3D printing technology. The experiment employed the same photo-reactive resin material to print a standard component for the test. Tensile and compression tests were conducted on the component to ascertain the mechanical properties of the photoreactive resin used in this study. The tensile tests were carried out using an Instron59 universal testing machine with a loading speed of 2 mm/min. Compression tests were performed on a Boyi 2025-100ST universal testing machine at a loading speed of 0.5 mm/min. The experiments revealed that the photoreactive resin material exhibits asymmetric behavior under tension and compression, with a tensile modulus of elasticity of 2240.6 MPa and a compressive modulus of elasticity of 824.6 MPa (see supplementary file fig.10 for details).

Data availability

All data are available from the corresponding author upon request. Source data are provided in this paper.

References

1. Pugnale, A. & Sassone, M. Structural reciprocity: critical overview and promising research/design issues. *Nexus Netw. J.* **16**, 9–35 (2014).
2. Popovic Larsen, O. Reciprocal Frame Architecture (1st ed.). Routledge. <https://doi.org/10.4324/9780080556000> (2007).
3. Hao, T. Architectural modeling design based on reciprocal structure. <https://doi.org/10.1051/e3sconf/202014301002> (2020).
4. Rizzuto, J. & Larsen, O. P. Connection systems in reciprocal frames and mutually supported elements space structure networks. *Int. J. Space Struct.* **25**, 243–256 (2010a).
5. Chea, C. P., Bai, Y., Fang, Y. & Zhang, Y. Geometric forming and mechanical performance of reciprocal frame structures assembled using fibre reinforced composites. *Eng. Struct.* **250**, 113420 (2022).
6. Allen, E., Zalewski, W., Michel, N. & Boston Structures Group. *Form and Forces: Designing Efficient, Expressive Structures*. (2010).
7. Kohlhammer, T. & Kotnik, T. Systemic behaviour of plane reciprocal frame structures. *Struct. Eng. Int.* **21**, 80–86 (2011).
8. Garavaglia, E., Pizzigoni, A., Sgambi, L. & Basso, N. Collapse behaviour in reciprocal frame structures. *Struct. Eng. Mech.* **46**, 533–547 (2013).
9. Popovic Larsen, O. Reciprocal frame (RF) structures: real and exploratory. *Nexus Netw. J.* **16**, 119–134 (2014).
10. Asefi, M. & Bahremandi-Tolou, M. Design challenges of reciprocal frame structures in architecture. *J. Build. Eng.* **26**, 100867 (2019).
11. Apolinarska, A. A., Kuhn, M., Gramazio, F. & Kohler, M. Performance-driven design of a reciprocal frame canopy - timber structure of the futuretree. <https://doi.org/10.52842/conf.ecaade.2021.1.497> (2021).
12. Asefi, M. & Tolou, M. B. Realization of historical persian ornamental and geometric patterns as architectural components in innovative reciprocal frame barrel vaults. *Int. J. Space Struct.* **36**, 180–196 (2021).
13. Gherardini, F. & Leali, F. Reciprocal frames in temporary structures: an aesthetical and parametric investigation. *Nexus Netw. J.* **19**, 741–762 (2017).
14. Parigi, D. & Pugnale, A. Three-dimensionality in reciprocal structures: concepts and generative rules. *Nexus Netw. J.* **16**, 151–177 (2014).
15. Baverel, O. & Pugnale, A. Reciprocal systems based on planar elements: morphology and design explorations. *Nexus Netw. J.* **16**, 179–189 (2014).
16. Baverel, O. & Larsen, O. P. A review of woven structures with focus on reciprocal systems - nexorades. *Int. J. Space Struct.* **26**, 281–288 (2011).
17. Thönnissen, U. A form-finding instrument for reciprocal structures. *Nexus Netw. J.* **16**, 89–107 (2014).
18. Douthe, C. & Baverel, O. Design of nexorades or reciprocal frame systems with the dynamic relaxation method. *Comput. Struct.* **87**, 1296–1307 (2009).
19. Pérez-Valcárcel, J., Suárez-Riestra, F., Muñoz-Vidal, M., López-César, I. & Freire-Tellado, M. J. A new reciprocal linkage for expandable emergency structures. *Structures* **28**, 2023–2033 (2020).
20. Gelez, S., Aubry, S. & Vaudeville, B. Nexorade or reciprocal frame system applied to the design and construction of a 850 M2 archaeological shelter. *Int. J. Space Struct.* **26**, 303–311 (2011).
21. Cucuzza, R., Aloisio, A., Rad, M. M. & Domaneschi, M. Constructability-based design approach for steel structures: From truss beams to real-world inspired industrial buildings. *Autom. Constr.* **166**, 105630 (2024).
22. Cucuzza, R., Rad, M. M., Domaneschi, M. & Marano, G. C. Sustainable and cost-effective optimal design of steel structures by minimizing cutting trim losses. *Autom. Constr.* **167**, 105724 (2024).
23. Zhao, J., Agkathidis, A., Lombardi, D. & Chen, H. Reinterpreting the Dougong joint: a systematic review of robotic technologies for the assembly of timber joinery. *Archit. Sci. Rev.* **68**, 65–79 (2024).

24. Olsen, C., & Mac Namara, S. *Collaborations in Architecture and Engineering* (2nd ed.). (Routledge, 2021). <https://doi.org/10.4324/9781003018179>.

25. Geno, J., Goosse, J., Van Nimwegen, S. & Latteur, P. Parametric design and robotic fabrication of whole timber reciprocal structures. *Autom. Constr.* **138**, 104198 (2022).

26. Kohlhammer, T., Apolinarska, A. A., Gramazio, F. & Kohler, M. Design and structural analysis of complex timber structures with glued T-joint connections for robotic assembly. *Int. J. Space Struct.* **32**, 199–215 (2017).

27. Parigi, D. & Kirkegaard, P. H. Design and fabrication of free-form reciprocal structures. *Nexus Netw. J.* **16**, 69–87 (2014).

28. Ilgin, H. E. & Günaydin, M. Contemporary tall residential timber buildings: what are the main architectural and structural design considerations? *J. Facilities Manag.* **17**, 245–262 (2019).

29. Epp, L. Vibration issues in timber structures: a state-of-the-art review. *Eng. Struct.* **174**, 123–135 (2018).

30. Castrionto, C. aioM., Celani, G. & Tavares, F. M. Reciprocal frames algorithm based on symmetry groups. *Nexus Netw. J.* **24**, 167–186 (2022). 2021.

31. Pérez-Valcárcel, J., Muñoz-Vidal, M., Suárez-Riestra, F., López-César, I. & Freire-Tellado, M. J. Deployable cylindrical vaults with reciprocal linkages for emergency buildings. *Structures* **33**, 4461–4474 (2021).

32. Chilton, J. *Development of Timber Reciprocal Frame Structures in the UK*. (2010).

33. P Xu, P Zhao, Y Liu, Reciprocal frame (RF) architecture design based on statistical analysis of geometrical form parameters from built cases and parametric simulations. *Constr. Build. Mater.* **447**, 138082 (2024).

34. Fang, D. et al. Modern timber design approaches for traditional Japanese architecture: analytical, experimental, and numerical approaches for the nuki joint. In *Proceedings of IASS Annual Symposia*. <https://infoscience.epfl.ch/server/api/core/bitstreams/7098fd91-1f31-4e32-8558-19965355fbc8/content> (2019).

35. Fang, D. & Mueller, C. Mortise-and-tenon joinery for modern timber construction: Quantifying the embodied carbon of an alternative structural connection. *Archit. Struct. Constr.* **3**, 11–24 (2023).

36. Hughes, T. J. R., Cottrell, J. A. & Bazilevs, Y. Isogeometric analysis: CAD, finite elements, NURBS, exact geometry and mesh refinement. *Comput. Meth. Appl. Mech. Eng.* **194**, 4135–4195 (2005).

37. Liu, Y., Yang, C., Wei, P., Zhou, P. & Du, J. An ODE-Driven Level-Set Density Method for Topology Optimization. *Computer Methods Appl. Mech. Eng.* **387**, 114159–114159 (2021).

38. Thomas, D. & Gilbert, S. W. Costs and cost effectiveness of additive manufacturing. <https://www.nist.gov/publications/costs-and-cost-effectiveness-additive-manufacturing>. (2021).

39. Neuman, E. The lightfall and the symbolic function of the hyperbolic paraboloid surface. *Nexus Netw. J.* **19**, 579–598 (2017).

40. Bäcklund, A. V. *Concerning Surfaces with Constant Negative Curvature*. (1905).

41. Elgohary, S. M., Abdin, A. R. & Mohamed, R. M. Performative driven form finding in the early design stage. *J. Eng. Appl. Sci.* **70**, 73 (2023).

42. Huang, Y., Xu, C. & Wang, L. A study of thermal performance enhancement of building envelopes by using corncob as construction material. *Sci. Rep.* **13**, 17891 (2023).

43. Kudela, J. & Matousek, R. Recent advances and applications of surrogate models for finite element method computations: A review. *Soft Comput.* **26**, 13709–13733 (2022).

44. Gao, X., Zhang, L. & Huang, X. Exploring spatial arrangement of locker area in ski resort hall for enhancing interpersonal distancing using unity engine. In *Proceedings of the 29th CAADRIA Conference*, **3**, 411–420 (2024).

45. Zhang, Z. et al. Construction of intelligent integrated model framework for the workshop manufacturing system via digital twin. *Int. J. Adv. Manuf. Technol.* **118**, 3119–3132 (2022).

46. Hu, Z., Wang, S. & Ma, C. Precision allocation method of large-scale CNC hobbing machine based on precision-cost comprehensive optimization. *Int. J. Adv. Manuf. Technol.* **126**, 3453–3474 (2023).

47. Hughes, R., Osterlund, T. & Larsen, N. M. Integrated design-for-manufacturing and AR-aided-assembly workflows for lightweight reciprocal frame timber structures. *Constr. Robot.* **5**, 147–157 (2021).

48. M. Larsson, H. Yoshida, T. Igarashi, Human-in-the-loop fabrication of 3D surfaces with natural tree branches. In *Proceedings of the ACM Symposium on Computational Fabrication*. (2019).

49. Sun, M. & Zhao, L. Impact of environmental regulatory types and green technological innovation on green total factor productivity in polluted areas of China. *Sustainability* **16**, 3871 (2024).

50. Sandak, A. Engineered living materials for sustainable and resilient architecture. *Nat. Rev. Mater.* **8**, 357–359 (2023).

51. Mishra, A. et al. Land use change and carbon emissions of a transformation to timber cities. *Nat. Commun.* **13**, 4889 (2022).

52. Design2machine, BTL. <https://design2machine.com/btl/index.html> (2021).

53. Zhang, S., Liu, N., Li, W. & Yan, S. Umbrella structure building design method via case-based design and statistical analysis of structural morphological parameters. *J. Build. Eng.* **45**, 103542 (2022).

Acknowledgements

The authors acknowledge the financial support from the National Natural Science Foundation of China (12272200) and the project of Beijing OptFuture Technology Co., Ltd (20212002316). The paper reflects the views and opinions of the authors, and not necessarily those of the funding entities. The authors also gratefully acknowledge the use of the image in Fig. 1f by Tom Podmore from Unsplash, licensed under the Unsplash License. The authors would like to thank Tsinghua University Architectural Design and Research Institute for kindly providing the image in Fig. 1f and granting permission for their use in this publication.

Author contributions

Conceptualization: P.X. and P.Z. Methodology: P.X., P.Z., B.X., and J.D. Investigation: P.X., P.Z., and Z.Z. Visualization: P.X., P.Z., and B.X. Funding acquisition: J.D. Supervision: J.D. and N.L. Writing – original draft: P.X. Writing – review & editing: P.X., P.Z., and S.Z.

Competing interests

The authors declare no competing interests.

Additional information

Supplementary information The online version contains supplementary material available at <https://doi.org/10.1038/s41467-025-66491-4>.

Correspondence and requests for materials should be addressed to Nianxiong Liu, Shuyang Zhang or Jianbin Du.

Peer review information *Nature Communications* thanks Raffaele Cucuzza and Denvid Lau for their contribution to the peer review of this work. A peer review file is available.

Reprints and permissions information is available at <http://www.nature.com/reprints>

Publisher's note Springer Nature remains neutral with regard to jurisdictional claims in published maps and institutional affiliations.

Open Access This article is licensed under a Creative Commons Attribution-NonCommercial-NoDerivatives 4.0 International License, which permits any non-commercial use, sharing, distribution and reproduction in any medium or format, as long as you give appropriate credit to the original author(s) and the source, provide a link to the Creative Commons licence, and indicate if you modified the licensed material. You do not have permission under this licence to share adapted material derived from this article or parts of it. The images or other third party material in this article are included in the article's Creative Commons licence, unless indicated otherwise in a credit line to the material. If material is not included in the article's Creative Commons licence and your intended use is not permitted by statutory regulation or exceeds the permitted use, you will need to obtain permission directly from the copyright holder. To view a copy of this licence, visit <http://creativecommons.org/licenses/by-nc-nd/4.0/>.

© The Author(s) 2025